IEEE Access
Multidisciplinary | Rapid Review | Open Access Journal

Received May 18, 2020, accepted July 20, 2020, date of publication July 31, 2020, date of current version August 10, 2020.

Digital Object Identifier 10.1109/ACCESS.2020.3013316

Structure Design and Image Reconstruction of Hexagonal-Array Photonics Integrated Interference Imaging System

CAN DING[1], XIANGCHAO ZHANG[1], (Member, IEEE), XINYUE LIU[2], HAORAN MENG[2], AND MIN XU[1]

[1]Academy for Engineering and Technology, Fudan University, Shanghai 200433, China
[2]Changchun Institute of Optics, Fine Mechanics and Physics, Chinese Academy of Sciences, Changchun 130033, China

Corresponding author: Xiangchao Zhang (zxchao@fudan.edu.cn)

This work was supported in part by the Fudan University-CIOMP Joint Fund under Grant FC2018-007, in part by the National Key Research and Development Program of China under Grant 2017YFB1104700, and in part by the National Natural Science Foundation of China under Grant 51875107.

ABSTRACT The photonics integrated interference imaging technique has attracted intensive attention because of its superior imaging performance and structural compactness. Traditional architecture designs of the photonics integrated interference imaging systems are of radial patterns and rectangular patterns. Due to their large lens intervals, the resulting frequency distributions are insufficient to satisfy the Nyquist sampling conditions. In this article, a new structural type of hexagonal arrays is designed, which has a dense lens distribution. Two paring methods are developed for the radial baselines and lateral baselines, and they can be selected according to the actual frequency bands of interest. The imaging performance of different arrays is analyzed, and the hexagonal array is proved superior over the radial pattern and rectangular pattern in terms of point spread functions. A reconstruction algorithm based on the compressed sensing theory is proposed to restore salient features from insufficiently sampled signals. A measurement matrix is set in accordance with the structural design to avoid data regridding. Experimental results demonstrate that the imaging resolution is improved remarkably with respect to the original images.

INDEX TERMS Interference imaging, baseline pairing, compressed sensing, image reconstruction.

I. INTRODUCTION

The resolution of a telescope is determined by the diffraction limit. With increasing demand for higher resolving capability, the apertures of the primary mirrors of astronomical telescopes are approaching tens of meters [1]. While the longitudinal length of the optical system is even greater than the mirror's aperture. For instance, the diameter of the Hubble Space Telescope's primary mirror is 2.4 m but its longitudinal length is 13.25 m [1]. A new type of telescope SPIDER (Segmented Planar Imaging Detector for Electro-optical Reconnaissance) is developed based on the interference imaging. Compared to the conventional electro-optical imaging systems, the size, weight, and power can be reduced by 10× to 100× for an equivalent imaging resolution by introducing photonic integrated circuits (PIC) [2], [3].

The associate editor coordinating the review of this manuscript and approving it for publication was Junjie Wu.

SPIDER contains two important components, namely the sensor system and the processing module. The sensor system is composed of a micro-lens array and the processing module is composed of PIC cards matched with the micro-lens array, both of which have significant impact on the imaging quality. Traditional architecture designs of SPIDER are of radial patterns, as illustrated in Fig.1. One-dimensional (1D) PIC cards distribute uniformly around an inner cylinder of a radius $r = b/[2\tan(\rho/2)]$, where b denotes the interval between two adjacent lenses. The angular space between two PIC cards is $\rho = 2\pi/k$, where k is the number of PIC cards. In the original system, k is set to be 27. Such a distribution leads to sparse arrangement of micro-lenses [4], [5].

The interference baselines formed by micro-lens pairs determine the spatial frequency of imaging, and the resolution is directly related to the longest baseline. The baseline pairing methods of the photonics integrated interference imaging system (PIIIS) are different from traditional interference antenna

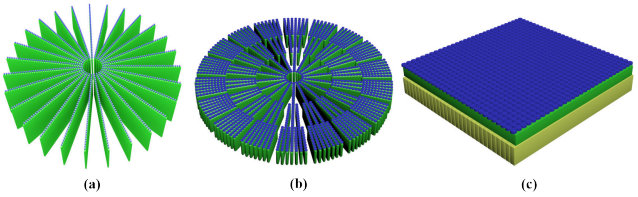

FIGURE 1. Traditional architecture designs of SPIDER (a) radial lens array; (b) hierarchical multistage lens array; (c) rectangular lens array.

arrays, because each lens can only form one baseline in the PIIIS, rather than being used repeatedly. Initially lenses are paired from the outer towards inner ones, i.e. lens 1 with N, 2 with N-1, and so on, where N is the number of lenses in a PIC card, henceforth the lengths of the baselines form an arithmetic sequence. The key components of the PIIIS chips such as arrayed waveguide gratings (AWGs) and multi-mode interferometer (MMIs) have a low integrating level, and the low frequency components are lacking, thus they cannot meet the requirement on the frequency coverage of high-quality imaging.

Subsequent researchers investigated various baseline pairing methods to achieve better image quality. Chu et al compared the high-frequency pairing method, low-frequency pairing method and uniform pairing method, and it is proved that the low-frequency pairing method is the best in terms of imaging quality, and a programmable baseline pairing method is developed to improve the feasibility and imaging quality in different scenarios [5]. In order to overcome the problem of insufficient sampling of low and medium frequencies, Gao et al proposed a hierarchical multistage lens array [6], as depicted in Fig.1(b). By increasing the number of lenses at the outermost layer and middle layer, the total numbers of short baselines and medium baselines can be increased.

With the improvement of integration ability of the PIC chips, large-scale arrays are demanded to acquire better image quality. Limited by the manufacturing capability, the complexity of the PIC system and henceforth the number of the spectral channels is restrained. However, improvement on the structure design and baseline pairing can adjust the frequency distribution, thus the imaging quality can be improved as well.

Owing to its superiority on miniaturization and compactness, an alternate structure of rectangular patterns is introduced, which contains 1D and two-dimensional (2D) PIC arrays [7], as depicted in Fig. 1(c). To overcome the lack of zero frequency, Yu et al proposed a ''checkerboard'' design and an aperture matching method, which can acquire a uniform frequency distribution together with the zero frequency [8]. Recently, Yang et al proposed a complex rectangular sub-aperture arrangement method to improve the imaging resolution further [9]. Rectangular patterns realize the dense arrangement of micro-lenses, which greatly increase the number of sampling points compared with the radial patterns.

Alternatively, reconstruction algorithms can be applied to improve the imaging quality numerically. Pratley et al proposed a reconstruction algorithm for the radial PIIIS inspired by the existing interference imaging technologies in the radio astronomy [10]. Regridding is conducted by interpolating the data, so that FFT can be implemented. However, this interpolating operation cannot be applied to nonlinear estimators such as power spectrum. In addition, the regridded data are correlated even if the original data are not [11]. As a consequence, serious reconstruction error can arise.

Recently, deep learning has attracted intensive attention because of its flexibility and widespread applications [12], but the reliability of the training results depends on the completeness and representativity of the training samples. It is difficult to collect comprehensive samples for PIIIS imaging at present. As a result, compressive sensing with proper sparse representations is adopted instead to break the Nyquist sampling limit of the subsampled frequency signals.

In this article, a hexagonal pattern is proposed. Then, two pairing methods are developed accordingly to switch between the high frequency mode and the mid-low frequency mode according to the actual requirements. A reconstruction algorithm is proposed based on the compressed sensing to improve the imaging resolution.

II. ANALYSIS OF IMAGING PERFORMANCE

The PIIIS is an interferometric system composed of micro-lenses and a PIC array. The micro-lens pattern is essentially a sparse aperture which couples light into the PIC array to realize interference imaging and its internal structure determines the baseline matching.

A. IMAGING PRINCIPLE

The imaging progress of the PIIIS is depicted in Fig.2. A parallel beam from a distant object propagates to the front surface of the micro-lens array. Two beams forming a baseline pass through the delay lines 1 and 2 in the waveguide, respectively, and interfere with each other in a four-quadrant orthogonal detector. The resulting intensity of the combined beam is

$$I = I_1 + I_2 + 2\sqrt{I_1 I_2}\,|\gamma_{12}| \times \cos\left\{\frac{2\pi}{\lambda}\left[\vec{L}\cdot\vec{B} + x_1 - x_2\right] + \arg(\gamma_{12})\right\} \quad (1)$$

where L is a unit vector in the direction of the incident parallel light, B is a baseline vector whose direction is from micro-lens 1 to micro-lens 2, and the dot product $L{\cdot}B$ represents the free space optical path difference from the object plane to the front surface of the micro-lens array. x_1 and x_2 are the optical path lengths through the interferometer associated with micro-lens 1 and micro-lens 2, respectively, and I_1 and I_2 denote the corresponding intensities. γ_{12} is the complex degree of coherence between the light collected in the two micro-lenses. The absolute value of visibility can be calculated as

$$\mathrm{abs}(V) = \frac{I_{\max} - I_{\min}}{I_{\max} + I_{\min}} = \frac{2\sqrt{I_1 I_2}}{I_1 + I_2}\,|\gamma_{12}| \quad (2)$$

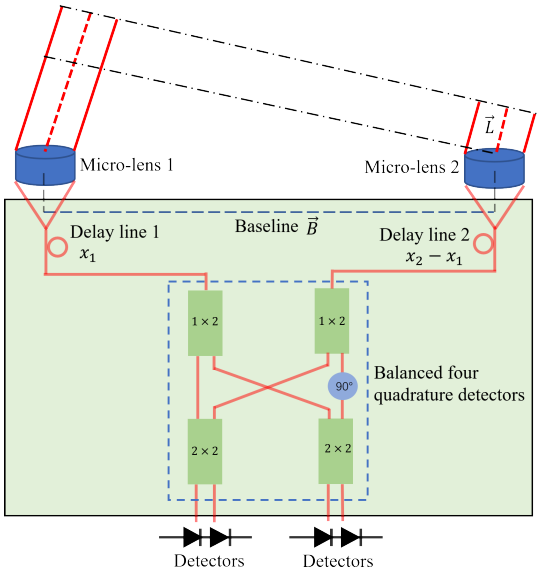

FIGURE 2. Diagram of imaging progress of PIIIS.

It is related to the source intensity through a Fourier transform relationship in accordance with the Van Cittert-Zernike theorem [13]. Images are formed by measuring the complex visibility from different baselines thereby building up an estimate of the two-dimensional Fourier transform of the source intensity distribution. The inverse Fourier transform of the complex visibility then yields the source intensity distribution.

B. POINT SPREAD FUNCTION

The optical performance of a micro-lens array can be assessed by its point spread function (PSF). An imaging system with sparse apertures is equivalent to a diffraction-limited incoherent imaging system [14]. PSF is hopefully close to the Dirac delta function, which has a narrow central peak and small-amplitude side lobes. The normalized PSF of the PIIIS is obtained by imaging an object at an infinite distance using a micro-lens array.

$$\begin{aligned} PSF\ (x,y) &= \left(\frac{\pi a^2}{\lambda f}\right)^2 \left\{\frac{2J_1\left[2\pi a\sqrt{x^2+y^2}/\lambda f\right]}{2\pi a\sqrt{x^2+y^2}/\lambda f}\right\}^2 \\ &\quad \times \left\{\sum_{n=1}^{N} \exp\left[-\frac{2\pi j}{\lambda f}\left(xx_n + yy_n\right)\right]\right\}^2 \\ &= PSF_d\ (x,y) \left\{\sum_{n=1}^{N} \exp\left[-\frac{2\pi j}{\lambda f}\left(xx_n + yy_n\right)\right]\right\}^2 \\ &= PSF_d\ (x,y) \left\{N + 2\sum_{j=1}^{N-1}\sum_{k=j+1}^{N} \right. \\ &\quad \left. \times \cos\left[\left(x_j - x_k\right)\frac{2\pi x}{\lambda f} + \left(y_j - y_k\right)\frac{2\pi y}{\lambda f}\right]\right\} \end{aligned} \quad (3)$$

where a is the radius of a single micro-lens, f is the focal length, λ is the wavelength of the incident light, J_1 is the first-order Bessel function, and PSF_d is the point spread function of the central micro-lens. (x, y) are the coordinates at the image plane, (x_n, y_n) are coordinates of the n-th micro-lens, and $(x_j\text{-}\ x_k)$, $(y_j\text{-}\ y_k)$ are coordinate shifts between two micro-lenses.

III. BASELINE PAIRING METHODS OF HEXAGONAL PIIIS

A hexagonal pattern is developed to combine 1D PIC chips and 2D PIC chips, which greatly increases the density of the micro-lens array compared to the radial patterns and rectangular ones. The fill factor is an important indicator for the imaging characteristics of micro-lens arrays, which refers to the ratio of the effective area to the total area of an equivalent single lens. The fill factor of sparse apertures is defined as $f = d/S$, where d is the diameter of a single micro-lens, and S is the average interval between two adjacent micro-lenses. Hexagonal arrays have larger fill factors, implying that hexagonal arrays have better compactness than the radial and rectangular arrays.

A. RADIAL PAIRING METHOD

Fig.3(a) depicts a hexagonal PIIIS, and Fig.3(b) shows the sub-bands in the micro-lens array. The lenses in the same color make up a sub-band. The central lens forms the first sub-band, and other sub-bands are defined from inner to outer rings in sequence.

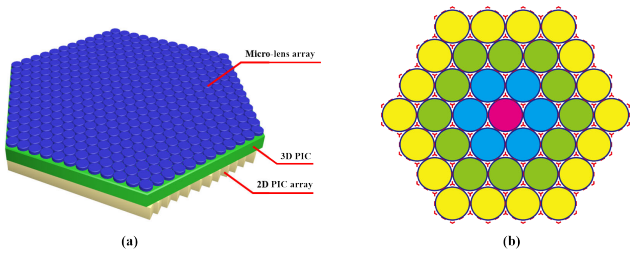

FIGURE 3. Hexagonal PIIIS's concept of design (a) 3D schematic; (b) lens rings.

The radial pairing method is shown in Fig. 4(a). A lens with coordinate (X, Y) composes a baseline with the farthest lens $(\text{-}X, \text{-}Y)$ in the same sub-band. As a result, the line linking a lens pair is along the radial direction. It is worth mentioning that the central lens (0, 0) is paired with itself to sample the zero frequency. The resulting length distribution and angular distribution of baselines are shown in Fig.4(b) and Fig.4(c), respectively. According to the formulae $u = \frac{\delta x}{\lambda z}$ and $v = \frac{\delta y}{\lambda z}$ [11], a long baseline corresponds to a high frequency, and a short baseline corresponds to a low frequency. Thus this radial pairing method can achieve the longest baseline in the hexagonal array. The frequency distribution (u, v) are made concentrated to high frequencies to obtain high resolution, but lack of low frequencies.

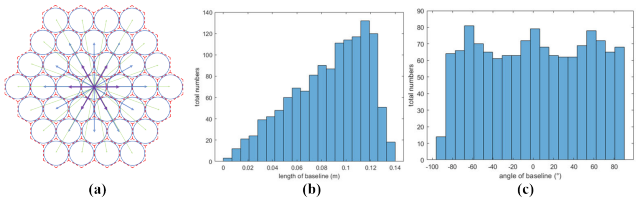

FIGURE 4. Distribution of baselines in radial pairing method (a) construction of baselines; (b) length distribution; (c) angle distribution (30 sub-bands; 2611 lenses; 1305 baselines).

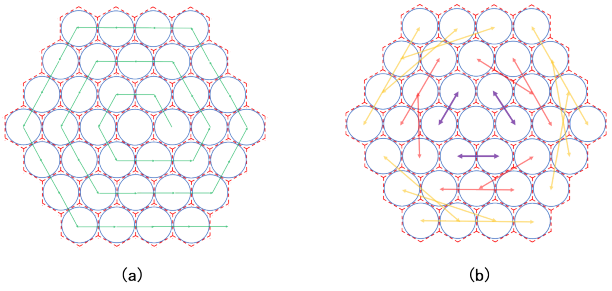

FIGURE 5. Lateral pairing method (a) spiral path; (b) construction of baselines.

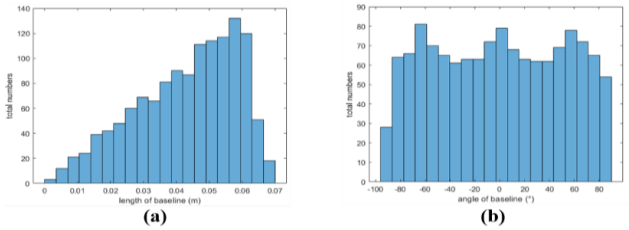

FIGURE 6. Distribution of baselines in lateral pairing method (a) length distribution; (b) angle distribution (30 sub-bands; 2611 lenses; 1305 baselines).

B. LATERAL PAIRING METHOD

A spiral path is designed in Fig.5(a). The path starts from the lens $(S, 0)$ in the second sub-band and then traverses counterclockwisely in sequence from lower sub-bands to higher ones. The search within a ring proceeds along the following six directions, namely $(i\text{-}2)S$ along 60°, $(i\text{-}1)S$ along 120°, 180°, 240° and 300°, and iS along 0°, respectively in the i-th sub-band.

The lateral pairing method is shown in Fig.5(b). The k-th lens in the i-th sub-band composes a baseline with the $(k + i\text{-}1)$-th lens along the spiral path. The length distribution and angular distribution of baselines are respectively shown in Fig.6(a) and Fig.6(b). It is obvious that the lateral pairing method is beneficial to the short and medium baselines, but disadvantageous for the long ones, implying that the frequency coordinates (u, v) are made concentrated to low frequencies and medium frequencies.

IV. IMAGE RECONSTRUCTION

According to the principle of the PIIIS, the imaging model is established as

$$g = H \cdot^* (AfA) + \eta \tag{4}$$

where g is the measured complex visibilities associated with different baselines, and f is the intensity distribution of the object to be solved.

The Fourier basis is chosen in the imaging model function A, because it is suited for describing the imaging process according to the Van Cittert-Zernike Theorem. Because A is a symmetric matrix in the case of the fast Fourier transform, the term AfA denotes the Fourier transform by rows and columns respectively. H is the sampling matrix of the PIIIS. It is composed of 0 and 1, corresponding to the sampled frequencies associated with different baselines. If the sampled complex visibility is not allocated exactly at a discrete frequency, fractional weights can be assigned to the neighboring frequencies. It is worth noting that the array multiplication between H and AfA does not require the sampled frequencies uniformly distributed, henceforth data regridding can be avoided. In actual measurements, a noise term η also needs to be considered due to the existence of atmospheric disturbance, CCD detecting noise and other errors.

PIIIS is suited to be applied in space exploration and military detection, and typically for imaging stars in dark sky, ships in the blue sea and so on. These salient features with remarkable gradient changes fortunately meet the representing capability of the compressed sensing theory [15]. To highlight the edges, a total variation term is added in the objective function as follows

$$\min_f \frac{\mu}{2}||H. * (AfA) - g||^2 + ||f||_{TV} \tag{5}$$

where $\frac{\mu}{2}\|H \cdot^* (AfA) - g\|^2$ is a similarity term used to indicate the difference between the calculated result and the measured spectrum. μ is the weighting coefficient, and $||f\ ||_{TV}$ is the total variation term used to measure the sharpness of edges

$$||f||_{TV} = ||\nabla f||_1 = ||Df||_1 + ||fD^T||_1$$

where D is the difference matrix. A 6×6 differentiation matrix is exemplified below

$$D = \begin{pmatrix} -1 & 1 & 0 & 0 & 0 & 0 \\ 0 & -1 & 1 & 0 & 0 & 0 \\ 0 & 0 & -1 & 1 & 0 & 0 \\ 0 & 0 & 0 & -1 & 1 & 0 \\ 0 & 0 & 0 & 0 & -1 & 1 \\ 0 & 0 & 0 & 1 & -3 & 2 \end{pmatrix}$$

Df means making difference row by row, and fD^T means making difference column by column.

Introduce intermediate variables s and t to convert the original non-differentiable problem into an equivalent optimization problem with equality constraints

$$\min_f \frac{\mu}{2}||H. * (AfA) - g||^2 + ||s||_1 + ||t||_1$$
$$\text{s.t.} \qquad s = Df,\ t = fD^T \tag{6}$$

The corresponding augmented Lagrangian problem is as follows

$$L(f,s,t,w,z) = \frac{\mu}{2}||H.*(AfA)-g||^2 + ||s||_1 + ||t||_1 - w(s-Df) - (t-fD^T)z + \frac{\rho_1}{2}||s-Df||^2 + \frac{\rho_2}{2}||t-fD^T||^2 \quad (7)$$

where w and z are Lagrangian multipliers, and ρ_1 and ρ_2 are penalty coefficients. It is difficult to directly solve the augmented Lagrangian problem, the alternating direction multiplier method (ADMM) can be employed by dividing the original problem into four sub-problems, where are straightforward to be solved [16],

$$f_{k+1} = \arg\min_f \frac{\mu}{2}\left\|H \cdot^* (AfA) - g\right\|^2 - w_k (s_k - Df) - \left(t_k - fD^T\right) z_k + \frac{\rho_1}{2}\|s_k - Df\|^2 + \frac{\rho_2}{2}\left\|t_k - fD^T\right\|^2$$

$$s_{k+1} = \arg\min_s \|s\|_1 - w_k^T (s - Df_{k+1}) + \frac{\rho_1}{2}\|s - Df_{k+1}\|^2$$

$$t_{k+1} = \arg\min_t \|t\|_1 - \left(t - f_{k+1}D^T\right) z_k^T + \frac{\rho_2}{2}\left\|t - f_{k+1}D^T\right\|$$

$$w_{k+1} = w_k - \rho_1 (s_{k+1} - Df_{k+1})$$

$$z_{k+1} = z_k - \rho_2 \left(t_{k+1} - f_{k+1}D^T\right)$$

The solving procedure of these sub-problems is presented as follows,

(1) f sub-problem

Differentiate with respect to f, and the resulting derivative formula is

$$2A[H^2.*(Af_{k+1}A) - H.*g]A + D^T w_k^{\mathrm{T}} + z_k^T D - \rho_1 D^T (s_k - Df_{k+1}) - \rho_2 (t_k - f_{k+1}D^T)D = 0 \quad (8)$$

(2) s and t sub-problems

The shrinkage formulae are adopted, and the solutions are given as

$$s_{k+1} = \max\left\{\left|Df_{k+1} + \frac{w_k}{\rho_1}\right| - \frac{1}{\rho_1}, 0\right\} sgn\left(Df_{k+1} + \frac{w_k}{\rho_1}\right) \quad (9)$$

$$t_{k+1} = \max\left\{\left|Df_{k+1} + \frac{z_k}{\rho_2}\right| - \frac{1}{\rho_2}, 0\right\} sgn\left(Df_{k+1} + \frac{z_k}{\rho_2}\right) \quad (10)$$

(3) w and z sub-problems

The solutions of these linear problems can be updated as

$$w_{k+1} = w_k - \rho_1(s_{k+1} - Df_{k+1}) \quad (11)$$

$$z_{k+1} = z_k - \rho_2(t_{k+1} - f_{k+1}D^T) \quad (12)$$

(4) ρ_1 and ρ_2 update

ρ_1 and ρ_2 can be set as fixed constants. However, a faster rate of convergence can be achieved by using the following parameter updating scheme

$$\rho_1 = \begin{cases} \gamma_1\rho_1 & \text{if} \|s_{k+1} - Df_{k+1}\|_2 \geq \alpha_1 \|s_{k+1} - Df_{k+1}\|_2 \\ \rho_1 & \text{otherwise} \end{cases}$$

$$\rho_2 = \begin{cases} \gamma_2\rho_2 & \text{if} ||t_{k+1} - f_{k+1}D^T||_2 \geq \alpha_2 ||t_{k+1} - f_{k+1}D^T||_2 \\ \rho_2 & \text{otherwise} \end{cases} \quad (13)$$

(5) Termination condition

$$\frac{||f_{k+1} - f_k||_2}{||f_k||_2} \leq tol$$

V. NUMERICAL DEMONSTRATION

In order to verify the imaging performance of the hexagonal micro-lens array, the PSFs associated with different numbers of sub-bands are calculated. The configuration parameters used are listed in Table 1.

TABLE 1. Configuration parameters of hexagonal array.

Parameter	Value
Wavelength	500 nm
Diameter of micro-lens	2.4 mm
Lens interval	2.9 mm
Object plane range	0.5 mm
Distance from pupil to image plane	0.5 m

The calculated PSFs associated with 2, 3, 4, 5, 10, and 20 sub-bands are shown in Fig. 7. The quantitative comparison of the normalized PSFs is depicted in Fig. 8. It is seen that as the number of sub-bands increases, the amplitude of side lobes decreases gradually, and the spot width shrinks significantly. When the number of sub-bands is greater than 10, high quality PSFs can be achieved.

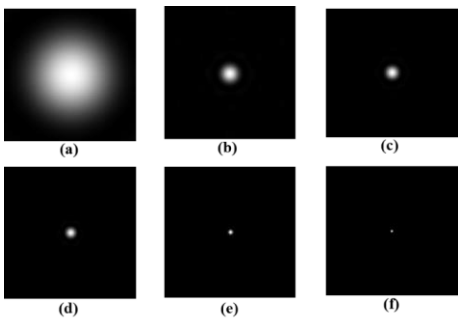

FIGURE 7. PSF of hexagonal PIIIS with different numbers of sub-bands (a) single lens; (b) 3 sub-bands; (c) 4 sub-bands; (d) 5 sub-bands; (e) 10 sub-bands; (f) 20 sub-bands.

Rectangular arrays and radial arrays with the same number of micro-lenses are adopted for comparison, as illustrated in Fig. 9, and the obtained PSFs are presented in Fig. 10. The same scale of rectangular array and hexagonal array have analogous geometric range (-0.04 m~0.04 m). While the hexagonal array has lower amplitude side lobes and narrower FWHM (full width at half maxima). This proves that hexagonal arrays have better imaging performance than rectangular ones. The radial distribution has a similar PSF with the hexagonal array, but by a cost of a much greater geometrical range (-0.1 m~0.1 m) due to the sparse arrangement of micro-lenses. Thus, a hexagonal micro-lens array is optimally distributed in terms of imaging performance.

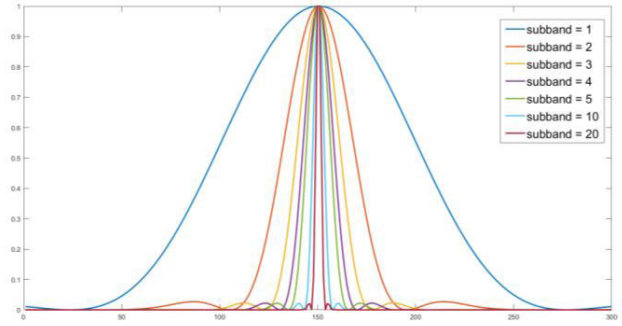

FIGURE 8. Comparison of PSFs of different numbers of sub-bands.

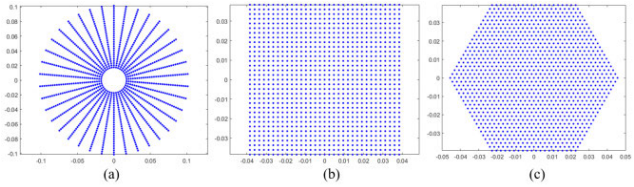

FIGURE 9. Three types of micro-lens arrays for PSF comparison (a) radial distribution (38 PIC cards and 30 micro-lenses per PIC cards, total lens number is 1140); (b) rectangular distribution (total lens number is 33 × 33 =1089); (c) hexagonal distribution (20 sub-bands, total lens number is 1141).

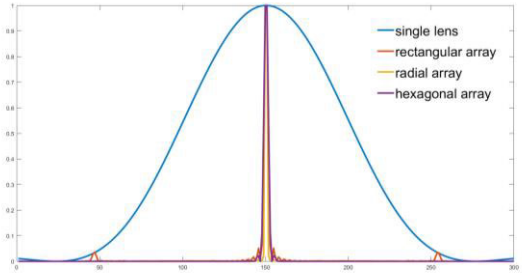

FIGURE 10. Comparison of PSFs of three micro-lens arrays.

TABLE 2. Configuration parameters for frequency assessment.

Parameter	Value
Diameter of micro-lens	2.4 mm
Wavelength range	300~1000 nm
Wavelength channel number	10
Object distance	50 km
Total number of micro-lens	2611

The broadband beam is split into 10 wavelength-channels in the AWGs, then the number of sampled frequencies can be increased. The frequency distributions of the two pairing methods of the hexagonal array are calculated using the configuration parameters listed in Table 2.

The spatial spectral range of the radial pairing method is (-0.4 cycles/m~0.4 cycles/m), as shown in Fig. 11. While the spatial spectral range in the lateral pairing method is (-0.2 cycles/m~0.2 cycles/m), as shown in Fig. 12. It is

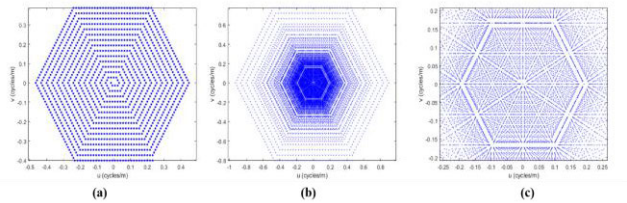

FIGURE 11. Frequency distribution of radial pairing method (a) frequency distribution at wavelength 600 nm); (b) frequency distribution of 10 wavelength channels; (c) Enlarged partial view of (b).

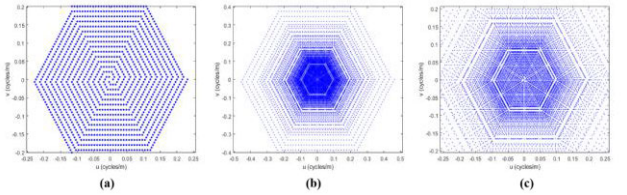

FIGURE 12. Frequency distribution of lateral pairing method (a) frequency distribution at wavelength 600 nm); (b) frequency distribution of 10 wavelength channels; (c) Enlarged partial view of (b).

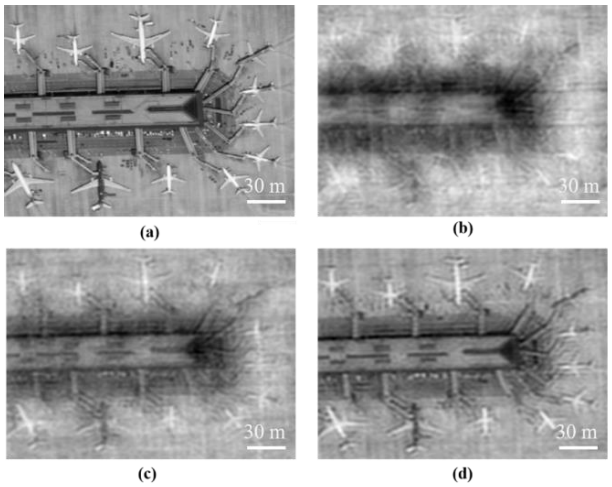

FIGURE 13. Images of hexagonal PIIIS (a) ground truth;(b) imaging result of 30 sub-bands; (c) imaging result of 40 sub-bands; (d) imaging result of 60 sub-bands. The scale bar is 30 m.

concluded that the radial pairing method is advantageous in collecting high frequencies, and conversely, the lateral pairing method is advantageous in collecting low frequencies. In different detection tasks, proper baseline pairing methods can be selected according to the demanded frequency distribution.

The imaging results of a hexagonal PIIIS using the radial baseline pairing method are shown in Fig. 13. It is clear that with the increase of the number of sub-bands, the image quality and resolution are improved significantly. The configuration parameters used are given in Table 3.

Due to the insufficient frequency sampling resulted from the limited baselines of hexagonal arrays, the imaging result is not clear. Then the reconstruction algorithm is applied. Fig.14 (a) and (b) are a target resolution board USAF 1951 and the direct imaging result by the hexagonal PIIIS with the radial pairing method. The limited number of

TABLE 3. Configuration parameters for imaging test.

Parameter	Value
Diameter of micro-lens	2.4 mm
Wavelength range	380~640 nm
Wavelength channel number	10
Object distance	50 km
Sub-band number	30, 40, 60

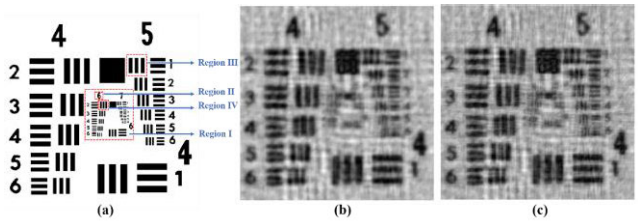

FIGURE 14. Reconstruction result of hexagonal PIIIS (a) ground truth; (b) direct imaging result; (c) reconstruction result.

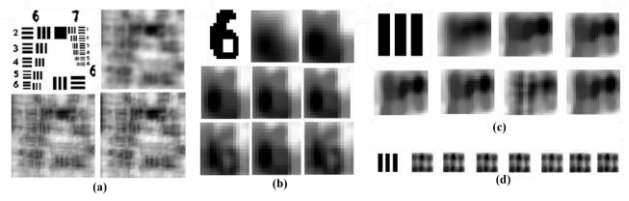

FIGURE 15. Impact of coefficient ρ on reconstruction quality (a) Region I (from top to bottom: target; imaging result; reconstruction result at $\rho = 14$; reconstruction result at $\rho = 40$); (b) Region II (from top to bottom: target; imaging result; reconstruction results at $\rho = 2, 6, 10, 14, 18, 40$; the clearest reconstruction result occurs at $\rho = 18$); (c) Region III (from top to bottom: target; imaging result; reconstruction results at $\rho = 2, 6, 10, 14, 18, 40$); (d) Region IV (From top to bottom: target; imaging result; reconstruction results at $\rho = 6, 10, 14, 18, 40, 70$).

TABLE 4. MSE and PSNR increments.

ρ	MSE	PSNR	PSNR increment
2	0.2483	6.0497	1.18%
6	0.2312	6.3595	6.36%
10	0.2275	6.4308	7.55%
14	0.2280	6.4209	7.38%
18	0.2161	6.6538	11.28%
40	0.2277	6.4260	7.47%

sub-bands leads to a lack of spatial frequencies, then the features are blurry and some details are unrecognizable. Fig.14(c) depicts the reconstruction result, with detailed morphologies improved remarkably. Fig. 15 shows that the resolutions of Regions I, II, III, and IV are improved significantly.

When using different penalty coefficients, the obtained image qualities are different. The mean-square error (MSE) and Peak Signal to Noise Ratio (PSNR) increment of Region II are given in Table 4 for quantitative comparison [17]. The perceptual quality based and semantic based metrics can also be applied for analysis.

VI. CONCLUSION

Due to its high fill factor, the interference imaging system with a hexagonal array can yield better imaging results. Appropriate baseline pairing methods can be applied according to the actual demanded frequency bands. But the numbers of micro-lenses and spectral channels are restricted by the actual fabricating capability and affordable cost of PIIISs, consequently the improvement of the imaging resolution by changing the physical structure is limited. As a natural alternative, numerical methods are investigated to improve the reconstruction quality. The Fourier bases are adopted in accordance with the imaging mechanism of PIIIS determined by the van Cittert-Zernike theorem, and a sampling matrix is assigned based on the actual frequency distribution of the captured complex visibilities. The operation of array multiplication is utilized to avoid data regridding. As a result, this reconstruction method does not require any mathematical assumption on the data models or error distributions. The resolution and imaging quality can be improved significantly.

ACKNOWLEDGMENT

The authors gratefully appreciate the helpful suggestions of Prof. Qinghua Yu from the Shanghai Institute of Technical Physics, Chinese Academy of Sciences.

REFERENCES

[1] I. Trumper, P. Hallibert, J. W. Arenberg, H. Kunieda, O. Guyon, H. P. Stahl, and D. W. Kim, "Optics technology for large-aperture space telescopes: From fabrication to final acceptance tests," *Adv. Opt. Photon.*, vol. 10, no. 3, pp. 644–702, 2018.
[2] R. L. Kendrick, A. Duncan, C. Ogden, J. Wilm, D. M. Stubbs, S. T. Thurman, T. Su, R. P. Scott, and S. J. B. Yoo, "Flat-panel space-based space surveillance sensor," in *Proc. Adv. Maui Opt. Space Surveill. Technol. Conf.*, 2013, pp. 1–9.
[3] R. P. Scott, T. Su, C. Ogden, S. T. Thurman, R. L. Kendrick, A. Duncan, R. Yu, and S. J. B. Yoo, "Demonstration of a photonic integrated circuit for multi-baseline interferometric imaging," in *Proc. IEEE Photon. Conf.*, Dec. 2014, pp. 1–2.
[4] V. C. du Foresto, S. Ridgway, and J.-M. Mariotti, "Deriving object visibilities from interferograms obtained with a fiber stellar interferometer," *Astron. Astrophys. Suppl. Ser.*, vol. 121, no. 2, pp. 379–392, Feb. 1997.
[5] Q. Chu, Y. Shen, M. Yuan, and M. Gong, "Numerical simulation and optimal design of segmented planar imaging detector for electro-optical reconnaissance," *Opt. Commun.*, vol. 405, pp. 288–296, Dec. 2017.
[6] W. Gao, X. Wang, L. Ma, Y. Yuan, and D. Guo, "Quantitative analysis of segmented planar imaging quality based on hierarchical multistage sampling lens array," *Opt. Express*, vol. 27, no. 6, pp. 7955–7967, 2019.
[7] A. Duncan, R. Kendrick, C. Ogden, D. Wuchenich, S. Thurman, S. J. B. Yoo, T. Su, S. Pathak, and R. Proietti, "SPIDER: Next generation chip scale imaging sensor," in *Proc. Adv. Maui Opt. Space Surveill. Technol. Conf.*, 2015, p. 27.
[8] Q. Yu, B. Ge, Y. Li, Y. Yue, F. Chen, and S. Sun, "System design for a 'checkerboard' imager," *Appl. Opt.*, vol. 57, no. 35, pp. 10218–10223, 2018.
[9] F. Yang, W. Yan, P. Tian, F. Li, and F. Peng, "Electro-optical imaging technology based on microlens array and fiber interferometer," *Appl. Sci.*, vol. 9, no. 7, pp. 1331–1341, Apr. 2019.
[10] L. Pratley and J. D. McEwen, "Sparse image reconstruction for the SPIDER optical interferometric telescope," 2019, *arXiv:1903.05638*. [Online]. Available: http://arxiv.org/abs/1903.05638
[11] E. Thiébaut and J.-F. Giovannelli, "Image reconstruction in optical interferometry," *IEEE Signal Process. Mag.*, vol. 27, no. 1, pp. 97–109, Jan. 2010, doi: 10.1109/MSP.2009.934870.
[12] G. Yang, S. Yu, and H. Dong, "DAGAN: Deep de-aliasing generative adversarial networks for fast compressed sensing MRI reconstruction," *IEEE Trans. Med. Imag.*, vol. 37, no. 6, pp. 1310–1321, Jun. 2018.

[13] T. Su, R. P. Scott, C. Ogden, S. T. Thurman, R. L. Kendrick, A. Duncan, R. Yu, and S. J. B. Yoo, "Experimental demonstration of interferometric imaging using photonic integrated circuits," *Opt. Express*, vol. 25, no. 11, pp. 12653–12665, 2017.
[14] R. D. Fiete, T. A. Tantalo, J. R. Calus, and J. A. Mooney, "Image quality of sparse-aperture designs for remote sensing," *Opt. Eng.*, vol. 41, no. 8, pp. 1957–1969, 2002.
[15] E. J. Candes and M. B. Wakin, "An introduction to compressive sampling," *IEEE Signal Process. Mag.*, vol. 25, no. 2, pp. 21–30, Mar. 2008.
[16] S. H. Chan, R. Khoshabeh, K. B. Gibson, P. E. Gill, and T. Q. Nguyen, "An augmented Lagrangian method for total variation video restoration," *IEEE Trans. Image Process.*, vol. 20, no. 11, pp. 3097–3111, Nov. 2011.
[17] J. Wang, R. Su, R. Leach, W. Lu, L. Zhou, and X. Jiang, "Resolution enhancement for topography measurement of high-dynamic-range surfaces via image fusion," *Opt. Express*, vol. 26, no. 26, pp. 34805–34819, 2018.

CAN DING received the B.E. degree from the School of Instrument Science and Opto-Electronics Engineering, Hefei University of Technology, in 2015. He is currently pursuing the master's degree with the School of Information Science and Technology, Fudan University. His research interests include super-resolution computational imaging and integrated photonics imaging.

XIANGCHAO ZHANG (Member, IEEE) received the B.E. degree in measurement technology from the University of Science and Technology of China, in 2005, and the Ph.D. degree in precision measurement and instrumentation from the University of Huddersfield, U.K., in 2009. Since 2011, he has been an Associate Professor with the Department of Optical Science and Engineering, Fudan University. His research interests include optical measurement technology, micro/nano optics, and image processing. He is a Senior Member of SPIE and a member of OSA.

XINYUE LIU received the B.Eng. degree in mechanical engineering from Tsinghua University, Beijing, China, in 1996, and the M.Eng. degree in mechatronics engineering and the Ph.D. degree in optical engineering from the University of Chinese Academy of Sciences, in 1999 and 2006, respectively. He is currently a Professor with the Changchun Institute of Optics, Fine Mechanics and Physics, Chinese Academy of Sciences. His research interests include interferometric metrology and imaging, aperture synthesis, and adaptive optics.

HAORAN MENG received the B.Eng. degree from Jilin University, China, in 2002, and the M.Eng. degree in optical engineering from the University of Chinese Academy of Sciences, in 2007. He is currently an Associate Professor with the Changchun Institute of Optics, Fine Mechanics and Physics, Chinese Academy of Sciences. He is engaged in the fields of optical interferometry, digital holography, and marine optics/ocean optics.

MIN XU received the M.S. and Ph.D. degrees in optical and electrical measurement science from Zhejiang University, China, in 1990 and 1998, respectively. Since 2008, he has been a Full Professor with the School of Information Science and Engineering, Fudan University. His research interests include the theory and application of the designing, manufacturing, and measuring of complex high-performance optical components. He is a Global Expert of the Thousand Talents Plan in China and the author of several patents for invention and over 100 publications in well-recognized journals and conferences.